Nonlinear Camera- and GNSS-Aided INS for Fixed-Wing UAV Using the eXogenous Kalman Filter

Lorenzo Fusini, Thor I. Fossen and Tor Arne Johansen

Abstract This chapter aims at applying a recently proposed estimator, called eXogenous Kalman Filter (XKF), to the navigation of a fixed-wing unmanned aerial vehicle (UAV) using inertial sensors, GNSS, and optical flow calculated from a camera. The proposed system is a cascade interconnection between a globally exponentially stable (GES) nonlinear observer (NLO) and a time-varying Kalman filter based on a local linearization of the system equations about the output of the preceding NLO. It is very well known that the linear time-varying Kalman filter is GES and optimal in the sense of minimum variance under some conditions, but when a nonlinear approximation (e.g., the extended Kalman filter) becomes necessary, generally such positive properties cannot be guaranteed anymore. On the other hand, a NLO often comes with strong, often global, stability properties, but without attention to optimality with respect to unknown measurement and process noise. The idea behind the XKF is to combine the advantages of the two composing estimators while surpassing the drawbacks from which they individually suffer. The theory is supported by tests on both simulated and experimental data, where the XKF is compared to a state-of-the-art solution based on the extended Kalman filter (EKF).

1 Background and Motivation

The problem of estimating the states of nonlinear systems has been approached in a large number of ways. The most popular and proficient tool has been the Kalman filter (KF) with its extensions. Under certain conditions, it guarantees optimal estimates

L. Fusini (✉) · T.I. Fossen · T.A. Johansen
Department of Engineering Cybernetics, NTNU Norwegian University of Science and Technology, Trondheim, Norway
e-mail: lorenzo.fusini@ntnu.no

T.I. Fossen
e-mail: thor.fossen@ntnu.no

T.A. Johansen
e-mail: tor.arne.johansen@ntnu.no

T.I. Fossen et al. (eds.), *Sensing and Control for Autonomous Vehicles*,
Lecture Notes in Control and Information Sciences 474,
DOI 10.1007/978-3-319-55372-6_2

in the sense of minimum variance, and its linear time-varying formulation is known to be globally exponentially stable [1, 22, 36]. When the system to observe is not linear, a linearized version is necessary. Linear approximation about a state estimate can be performed using different techniques, leading to variants of the KF such as the extended KF, unscented KF, Monte Carlo filter, and particle filter [6, 10, 13, 21]. The global stability properties of the resulting filters might not be guaranteed anymore, as they usually depend on implicit conditions that cannot be verified on the linearized system [32, 37].

The estimation of position, velocity, and attitude is a fundamental task in navigation of UAVs. Since the early 1990s [33], the field has seen the rise and development of nonlinear observers as substitutes for Kalman filters. Particular effort has been put in attitude estimation, which is typically performed by comparing a set of vectors measured in the body-fixed coordinate frame with a set of reference vectors in a reference frame [2, 3, 15, 28, 30], while others have also included the estimation of position and velocity [12, 17, 20]. A typical payload of sensors for navigation includes, but is not limited to, IMU, magnetometers, and GNSS receiver.

The use of nonlinear observers is attractive because they often come with globally exponential stability properties, which guarantee a correct behavior in the presence of uncertain initialization or unknown disturbances, and because their computational footprint is small as a consequence of the reduced number of differential equations involved. The design, however, does not take into account properties of the noise affecting both the system model and the measurements, resulting in suboptimal estimates.

The work presented here analyzes the properties and performance of a cascade interconnection between a GES NLO and a linear time-varying Kalman filter (LKF), and provides performance results based on experimental data. The objective is to build an estimator that inherits the advantages of the constituting components and discards their shortcomings. This method, called eXogenous Kalman filter (XKF), was presented and its properties formally analyzed in [19], and tested on simulated systems for both aerial and underwater vehicles [17, 39]. Here it is applied to a camera-aided inertial navigation system for a UAV: the NLO stage is a variation of the GES observer used in [12], it uses velocity and acceleration vectors in its output injection term [9], and it is then connected to a LKF to build the proposed XKF, and formally analyzed to conclude on its GES properties. Subsequently, it is tested on experimental data collected during the flight of a fixed-wing UAV and compared to the output of an EKF and of the NLO stage. As perfect reference values are not available in the experimental data, additional simulations are presented to provide another comparison between NLO, XKF, and EKF.

A fundamental component of the NLO is its body-referenced velocity, which is calculated by means of the optical flow extracted from the camera images and the information obtained by some of the other sensors available. The method was discussed in detail in [9], and a summary is reported here.

An alternative NLO is also tested, with the velocity vectors replaced by another pair of vectors that also exploits the GNSS measurements; it can be a useful, temporary solution in case faults appear in the system and invalidate the body-referenced velocity vector.

2 Notation and Measurements

Vectors and matrices are represented by lowercase and uppercase letters, respectively. X^{-1} and X^{+} denote the inverse and pseudoinverse of a matrix, respectively, and X^{T} the transpose of a matrix or vector. The symbols $\bar{x}$ and $\hat{x}$ indicate the estimate of x as output by the NLO and XKF, respectively, and $\breve{x} = x - \bar{x}$ and $\tilde{x} = x - \hat{x}$ the respective estimation errors. The operator $\|\cdot\|$ denotes the Euclidean norm for vectors and the Frobenius norm for matrices, I_n is the identity matrix of order n, and $0_{m\times n}$ is the $m \times n$ matrix of zeros. The function $\text{sat}(\cdot)$ performs a component-wise saturation of its vector or matrix argument to the interval $[-1, 1]$. The operator $S(x)$ transforms the vector x into the skew-symmetric matrix

$$S(x) = \begin{bmatrix} 0 & -x_3 & x_2 \\ x_3 & 0 & -x_1 \\ -x_2 & x_1 & 0 \end{bmatrix}$$

The inverse operation is denoted as $\text{vex}(\cdot)$, such that $\text{vex}(S(x)) = x$. For a square matrix A, its skew-symmetric part is represented by $\mathbb{P}_a(A) = \frac{1}{2}(A - A^T)$.

The reference frames considered in the paper are the body-fixed frame {B}, the North-East-Down (NED) frame {N} (Earth-fixed, considered inertial) and the camera frame {C}. The rotation from frame {B} to {N} is represented by the matrix $R_b^n \equiv R \in SO(3)$, where $SO(3)$ represents the Special Orthogonal group of dimension 3. The camera is assumed to be fixed to the body and perfectly aligned to its axes, so the camera frame and body frame represent the same coordinate system and can be identified by {B} alone.

A vector decomposed in {B} and {N} has superscript ^{b} and ^{n} respectively. The body (camera) location w.r.t. {N} is described by $c^n = [c_x^n, c_y^n, c_z^n]^T$. A point in the environment expressed w.r.t. {N} is $t^n = [x^n, y^n, z^n]^T$: note that a point located at the mean sea level corresponds to $z^n = 0$, and such it will be considered throughout the paper. The same point expressed w.r.t. {B} is $t^b = [x^b, y^b, z^b]^T$. It will also be assumed that every point representing a feature captured by the camera is fixed w.r.t. {N}. The gravity vector is defined as $g^n = [0, 0, g]$, with g the local gravitational acceleration. The greek letters ϕ, θ, and ψ represent the roll, pitch, and yaw angles respectively, defined according to the zyx convention for principal rotations [7]. A 2-D camera image has coordinates $[r, s]^T$, aligned with the y^b- and z^b-axis respectively (see Fig. 2). The derivative $[\dot{r}, \dot{s}]^T$ of the image coordinates is the optical flow (OF).

2.1 Measurements

The experimental sensor suite consists of the following units:

- *GNSS receiver*: NED position p^n and velocity v^n;
- *IMU*: biased angular velocity $\omega_m^b = \omega^b + b^b$, where b^b represent the bias, and specific force f^b, which is assumed bias-compensated by using, for example, the method in [11];
- *machine vision based on downward-facing camera*: body-fixed velocity v^b;
- *altimeter*: height over ground c_z^n;
- *inclinometers*: roll ϕ and pitch θ angles measurements.

3 Machine Vision

A machine vision system is designed to calculate the body-fixed velocity v^b from information available from camera, GNSS, altimeter, and inclinometers. A detailed description of the method is found in [9, 29], while its most relevant aspects for the present application are reported here.

3.1 Optical Flow

There exist several methods for computing the OF; for the present work, two specific methods are combined. The first one is SIFT [26], which provided the overall best performance in [29]. The total number of OF vectors in each image depends on the number of features detected and matched together. Since the transformation in Sect. 3.2 requires at least three OF vectors [9], it is necessary to make sure that this is handled. SIFT does not guarantee three distinct OF vectors since relatively homogeneous environments, such as snow or the ocean, increase the difficulty of finding distinct features. Therefore, the OF vectors created by SIFT are combined with a second method, which is based on region matching [8].

The region matching method used here is a template matching approach based on normalized cross-correlation [34]. The displacements of twelve templates, created symmetrically across the images, are used to find twelve OF vectors. Template matches below a given threshold are discarded and the corresponding OF vector is not used. Unreliable matches can occur in case of homogeneous terrain, changes in brightness or simply when the area covered by the template has disappeared from the image in the time between the capture of images. An example of OF vectors computed with SIFT and template matching is displayed in Fig. 1.

Erroneous OF vectors are detected in case of mismatches, so it is desired to locate and remove these vectors. For this reason, an outlier detector is implemented before the vectors are used to calculate the body-fixed velocity. The outlier detector utilizes

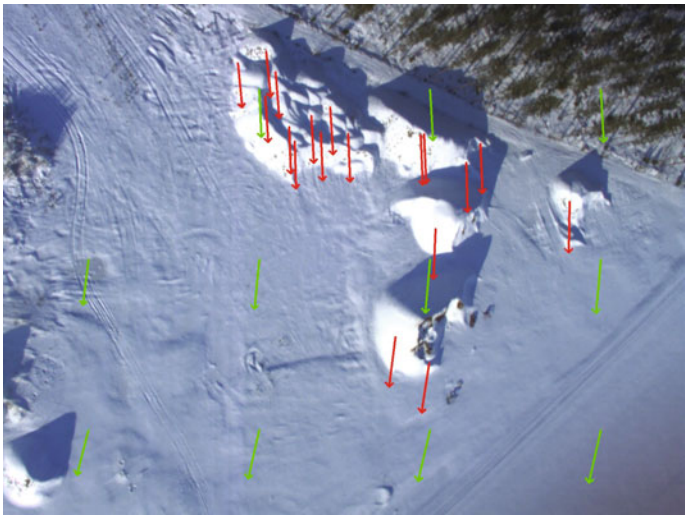

Fig. 1 Optical flow vectors. The *red ones* are generated by SIFT, the *green ones* by template matching

a histogram to find the vectors that deviate from the median with respect to direction and magnitude.

3.2 From Optical Flow to Body Velocity

For the OF computations to be useful as observer measurements, a transformation to body-fixed velocity is necessary. The pinhole camera model is used [16, 38]: despite being an ideal model, it gives results that are good enough for the purpose of this work. The camera-fixed frame is related to the body-fixed frame as illustrated in Fig. 2, where the optical axis of the downward-looking camera is aligned with the body z-axis. The focal point of the camera is assumed to coincide with the origin of $\{\mathrm{B}\}$.

The relationship between a point on the terrain $t^b = [x^b, y^b, z^b]^T$ and its projection onto the image plane $[r, s]^T$ is, according to the pinhole camera model,

$$\begin{bmatrix} r \\ s \end{bmatrix} = \frac{f}{z^b} \begin{bmatrix} y^b \\ -x^b \end{bmatrix}, \quad z^b \neq 0 \tag{1}$$

where f is the focal length of the camera. As t^b in itself is not available, a transformation [9, 29] is used to express t^b as a function of roll, pitch, height over ground, image features, and camera focal length

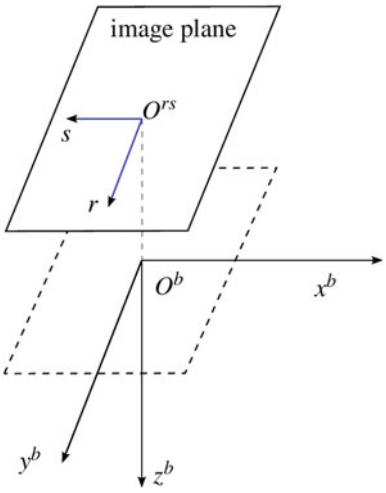

Fig. 2 Pinhole camera model. The camera is oriented downwards, while x^b is the direction of flight. O^{rs} and O^b are the origins of the image plane and body frame, respectively

$$\begin{bmatrix} x^b \\ y^b \\ z^b \end{bmatrix} = \begin{bmatrix} \frac{sc_z^n}{s\sin(\theta)+\cos(\theta)(f\cos(\phi)+r\sin(\phi))} \\ -\frac{rc_z^n}{s\sin(\theta)+\cos(\theta)(f\cos(\phi)+r\sin(\phi))} \\ -\frac{fc_z^n}{s\sin(\theta)+\cos(\theta)(f\cos(\phi)+r\sin(\phi))} \end{bmatrix} \tag{2}$$

All features tracked by the camera are assumed to be stationary with respect to {N}, therefore the UAV's linear and angular velocities, v^b and ω^b, relative to a feature tracked by the OF algorithm will be equal for every tracked feature at a given instant in time. Furthermore, it is assumed that the terrain is flat, such that every feature is located at the same altitude: this simplifies the analysis and is a reasonable assumption for the experiment considered here, as the results show; for rough terrains, other approaches are necessary [14].

For every feature j, the relationship between OF and body-fixed linear/angular velocity is given as

$$\begin{bmatrix} \dot{r}_j \\ \dot{s}_j \end{bmatrix} = -M_j(f, r_j, s_j, \phi, \theta, c_z^n) \begin{bmatrix} v^b \\ \omega^b \end{bmatrix} \tag{3}$$

$$M_j = \frac{f}{z_j^b} \begin{bmatrix} 0 & 1 & -\frac{y_j^b}{z_j^b} & -\frac{{y_j^b}^2}{z_j^b} - z_j^b & \frac{y_j^b x_j^b}{z_j^b} & x_j^b \\ -1 & 0 & \frac{x_j^b}{z_j^b} & \frac{x_j^b y_j^b}{z_j^b} & -\frac{{x_j^b}^2}{z_j^b} - z_j^b & y_j^b \end{bmatrix} \tag{4}$$

where $M_j \in \mathbb{R}^{2\times 6}$ is derived in [9]. The parameters in (3) on which M_j depends appear explicitly after substituting the variables in (4) with (2). If the number of features being tracked is k, then the OF vector has dimension $2k$. A matrix $M \in \mathbb{R}^{2k\times 6}$ can be created by concatenating the matrices M_j, $j = 1 \ldots k$, vertically, such that each feature j adds two rows to M, and by calculating the pseudoinverse of M, the

angular and linear velocities can be computed as

$$\begin{bmatrix} v^b \\ \omega^b \end{bmatrix} = -M^+ \begin{bmatrix} \dot{r}_1 \\ \dot{s}_1 \\ \vdots \\ \dot{r}_k \\ \dot{s}_k \end{bmatrix} \tag{5}$$

All the parameters constituting M are known, since they are either measured $(r_j, s_j, \phi, \theta, c_z^n)$ or known upon assembling the payload (f). M^+ exists only if $M^T M$ has full rank, such that it can be expressed as $M^+ = (M^T M)^{-1} M^T$. This can only happen if the number of flow vectors is greater than or equal to three.

4 Design and Analysis

The NLO and LKF are designed around two slightly different versions of the strapdown navigation equations, the difference being how the attitude of the UAV is parameterized. In the NLO, the attitude is parameterized as a rotation matrix with nine degrees of freedom, whereas the LKF uses Euler angles defined according to the *zyx* convention for principal rotations [7]. The NLO uses the rotation matrix in order to achieve a GES estimation error, but in the LKF this is replaced by Euler angles to take advantage of the reduced number of states, which have a direct impact on the computational footprint of the system. Additional details will be explained in the following Sections.

4.1 Nonlinear Observer

When designing the NLO, the kinematic system to observe can be divided into an attitude part $\Sigma_{A_{NLO}}$ and a translational motion part $\Sigma_{TM_{NLO}}$. Their equations are

$$\Sigma_{A_{NLO}} \begin{cases} \dot{R} = RS(\omega_m^b - b^b) \\ \dot{b}^b = 0 \end{cases} \tag{6}$$

$$\Sigma_{TM_{NLO}} \begin{cases} \dot{p}^n = v^n \\ \dot{v}^n = Rf^b + g^n \end{cases} \tag{7}$$

The following assumptions are made:

Assumption 1 A sufficient number of distinct image features are selected, such that M has full rank and its pseudoinverse can be calculated as $M^+ = (M^T M)^{-1} M^T$.

Assumption 2 The gyro bias b^b is constant, and there exists a known constant $L_b > 0$ such that $\|b^b\| \leq L_b$.

Assumption 3 There exists a constant $c_{obs} > 0$ such that, $\forall t \geq 0$, $\|f^b \times v^b\| \geq c_{obs}$.

Assumption 3 imposes the noncollinearity of the vectors v^b and f^b, i.e., the angle between them is nonzero and none of them can be identically zero. f^b is the specific force measured by the IMU, and the gravity vector is also measured by said sensor, so that a UAV flying at constant speed has $f^b = -R^T g^n$. In addition, a fixed-wing UAV always has a positive forward speed during flight and typically never accelerates just in the direction of g^n, so that Assumption 3 is never violated. If, on the other hand, a helicopter-like vehicle is used, it often finds itself hovering or moving perpendicular to the ground, situations that would violate Assumption 3. Caution must be exercised if the NLO is tested on vehicles other than fixed-wing UAVs.

Nonlinear Observer Equations

The NLO, graphically represented in Fig. 3, is based on the method proposed by [12] and is chosen as

$$\bar{\Sigma}_{A_{NLO}} \begin{cases} \dot{\bar{R}} = \bar{R} S(\omega_m^b - \bar{b}^b) + \sigma K_P J \\ \dot{\bar{b}}^b = \text{Proj}(\bar{b}^b, -k_I \text{vex}(\mathbb{P}_a(\bar{R}_s^T K_P J))) \end{cases} \tag{8}$$

$$\bar{\Sigma}_{TM_{NLO}} \begin{cases} \dot{\bar{p}}^n = \bar{v}^n + K_{pp}(p^n - \bar{p}^n) + K_{pv}(v^n - \bar{v}^n) \\ \dot{\bar{v}}^n = \bar{f}^n + g^n + K_{vp}(p^n - \bar{p}^n) + K_{vv}(v^n - \bar{v}^n) \\ \dot{\xi} = -\sigma K_P J f^b + K_{\xi p}(p^n - \bar{p}^n) + K_{\xi v}(v^n - \bar{v}^n) \\ \bar{f}^n = \bar{R} f^b + \xi \end{cases} \tag{9}$$

The subsystem $\bar{\Sigma}_{A_{NLO}}$ represents the attitude observer, in which K_P is a symmetric positive definite gain matrix, $\sigma \geq 1$ is a scaling factor that can be tuned to guarantee stability, k_I is a positive scalar gain, $\bar{R}_s = \text{sat}(\bar{R})$, and $\text{Proj}(\cdot, \cdot)$ represents a parameter

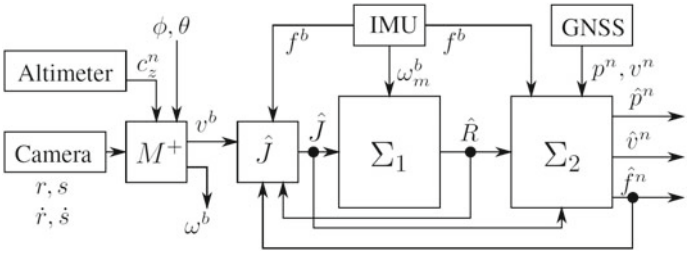

Fig. 3 Block diagram of the nonlinear observer

projection [24] that ensures that $\|\bar{b}^b\|$ does not exceed a design constant $L_{\bar{b}} > L_b$ (see Appendix). The matrix J is the output injection representing the attitude error, whose design is inspired by the TRIAD algorithm [35]. It is defined as

$$J(f^b,\ \bar{f}^n, v^b, v^n, \bar{R}) := \bar{A}_n A_b^T - \bar{R} A_b A_b^T \tag{10a}$$

$$A_b := \left[f^b,\ f^b \times v^b,\ f^b \times (f^b \times v^b)\right] \tag{10b}$$

$$\bar{A}_n := \left[\bar{f}^n,\ \bar{f}^n \times v^n,\ \bar{f}^n \times (\bar{f}^n \times v^n)\right] \tag{10c}$$

The body-fixed velocity vector v^b is calculated by means of the OF, according to (5).

The subsystem $\bar{\Sigma}_{TM_{NLO}}$ represents the translational motion observer, where K_{pp}, K_{pv}, K_{vp}, K_{vv}, $K_{\xi p}$, and $K_{\xi v}$ are observers gains yet to be defined. The presence of the term ξ lets the error dynamics of (9) be linear, which simplifies the analysis of stability.

The error dynamics of (8)–(9) can be written as

$$\breve{\Sigma}_{A_{NLO}} \begin{cases} \dot{\breve{R}} = RS(\omega^b) - \bar{R}S(\omega_m^b - \bar{b}^b) - \sigma K_P J \\ \dot{\breve{b}}^b = -\text{Proj}(\bar{b}^b, \tau(J)) \end{cases} \tag{11}$$

$$\breve{\Sigma}_{TM_{NLO}} \begin{cases} \dot{\breve{p}}^n = \breve{v}^n - K_{pp}\breve{p}^n - K_{pv}\breve{v}^n \\ \dot{\breve{v}}^n = \breve{f}^n - K_{vp}\breve{p}^n - K_{vv}\breve{v}^n \\ \dot{\breve{f}}^n = -K_{\xi p}\breve{p}^n - K_{\xi v}\breve{v}^n + \breve{d} \end{cases} \tag{12}$$

where $\tau(J) = -k_I \,\text{vex}(\mathbb{P}_a(\bar{R}_s^T K_P J))$ and $\breve{d} = (RS(\omega^b) - \bar{R}S(\omega_m^b - \bar{b}^b))f^b + (R - \bar{R})\dot{f}^b$. By defining the error state $\breve{w} = [(\breve{p}^n)^T, (\breve{v}^n)^T, (\breve{f}^n)^T]^T$, the error dynamics (12) can be written in a more compact form as

$$\dot{\breve{w}} = (A - KC)\breve{w} + B\breve{d} \tag{13}$$

where

$$A = \begin{bmatrix} 0_{6\times 3} & I_6 \\ 0_{3\times 3} & 0_{3\times 6} \end{bmatrix}, \qquad B = \begin{bmatrix} 0_{6\times 3} \\ I_3 \end{bmatrix},$$

$$C = \begin{bmatrix} I_6 & 0_{6\times 3} \end{bmatrix}, \qquad K = \begin{bmatrix} K_{pp} & K_{pv} \\ K_{vp} & K_{vv} \\ K_{\xi p} & K_{\xi v} \end{bmatrix}.$$

The NLO just presented differs from the one in [12] in how (10) is defined, that is the magnetic field vectors are replaced by the OF velocity vectors.

Stability Analysis

Theorem 1 defines the conditions that render the equilibrium of (11)–(12) globally exponentially stable (GES).

Theorem 1 *Let σ be chosen sufficiently large and define $H_K(s) = (Is - A + KC)^{-1}B$. There exists a $\gamma > 0$ such that, if K is chosen such that $A - KC$ is Hurwitz and $\|H_K(s)\|_\infty < \gamma$, then the origin of the error dynamics (11)–(12) is GES. Moreover, K can always be chosen to satisfy these conditions.*

Proof See the proof of Theorem 3 in [12]. The magnetic field vectors are replaced by the OF velocity vectors, but since both v^b and v^n are measured quantities, the analysis remains unchanged under Assumptions 1–3. □

It is clear that the only uncertainty considered in the design and analysis of the NLO is the gyro bias, while all the high-frequency noise components affecting the system can be entirely disregarded, despite being present. This constitutes an advantage of the NLO over Kalman filter designs, as already anticipated in Sect. 1, but at the same time it offers no insight into the behavior of the variance of the estimation error. This is addressed in Sect. 4.2.

4.2 Exogenous Kalman Filter

One of the most popular tools for state estimation and filtering in navigation is the EKF, which linearizes the system to observe about the trajectory estimated by the filter itself, but whose stability properties are not clear due to its feedback structure. The XKF, conversely, linearizes the same system about the trajectory estimated by the NLO, which is guaranteed to be GES, and has a cascade structure (see Fig. 4). Since the linearization is made about an exogenous state trajectory, there is no feedback loop that can destabilize the second-stage LKF, and it follows from nonlinear stability theory that the cascade interconnection inherits the stability properties of the global NLO [19, 25, 31].

Observed System and Filter Equations

In order to reduce the number of states, the kinematic system considered for this second-stage filter is represented slightly differently from (6)–(7), as

$$\dot{\Theta} = T(\Theta)(\omega_m^b - b^b + n_\omega) \tag{14a}$$
$$\dot{b}^b = n_b \tag{14b}$$
$$\dot{p}^n = v^n \tag{14c}$$
$$\dot{v}^n = R(f^b + n_s) + g^n \tag{14d}$$

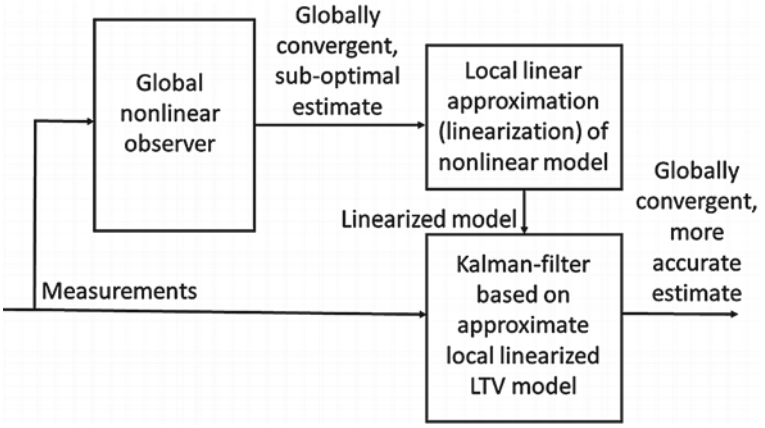

Fig. 4 Block diagram showing the cascade interconnection between an NLO and LKF, compactly called XKF, [19]

The attitude is now represented by the vector of Euler angles $\Theta = [\phi, \theta, \psi]^T$ with its dynamic equation, where $T(\Theta) \in \mathbb{R}^{3\times3}$ is the state-dependent transformation matrix [7]. n_b represents the process noise on the bias dynamics, and n_ω and n_s are noise on gyroscopes and accelerometers, respectively.

The output vector $y = [y_1, y_2, y_3, y_4]^T$ is necessary to implement the XKF. The measurements used to build y are position (GNSS), NED velocity (GNSS), body velocity (machine vision), and specific force (IMU), and are related to the states of the system via

$$y_1 = p^n + n_p \qquad \text{GNSS} \tag{15a}$$
$$y_2 = v^n + n_{v^n} \qquad \text{GNSS} \tag{15b}$$
$$y_3 = R^T v^n + n_{v^b} \qquad \text{machine vision} \tag{15c}$$
$$y_4 = -R^T g^n + (\omega_m^b - \hat{b}^b + n_\omega) \times (v^b + n_{v^b}) + n_s \qquad \text{IMU} \tag{15d}$$

The quantities n_p, n_{v^b}, and n_{v^n} represent noise on the sensors. All noise components in (14)–(15) are assumed to be Gaussian white noise. Note that (15d) is obtained from

$$f^b = -R^T g^n + \omega^b \times v^b + \dot{v}^b \tag{16}$$

It is common in navigation to consider only $f^b = -R^T g^n$, which might not yield accurate results in systems with high dynamics such as UAVs, for which the centripetal acceleration $\omega^b \times v^b$ is not neglectable. To verify the validity of this claim, Fig. 5 illustrates the norms of the three terms on the right-hand side of (16) as obtained during the flight test. It is clear that $\omega^b \times v^b$ contributes significantly to f^b, whereas $\dot{v}^b$ is always smaller and can be neglected. The peaks in $\omega^b \times v^b$ correspond to turns

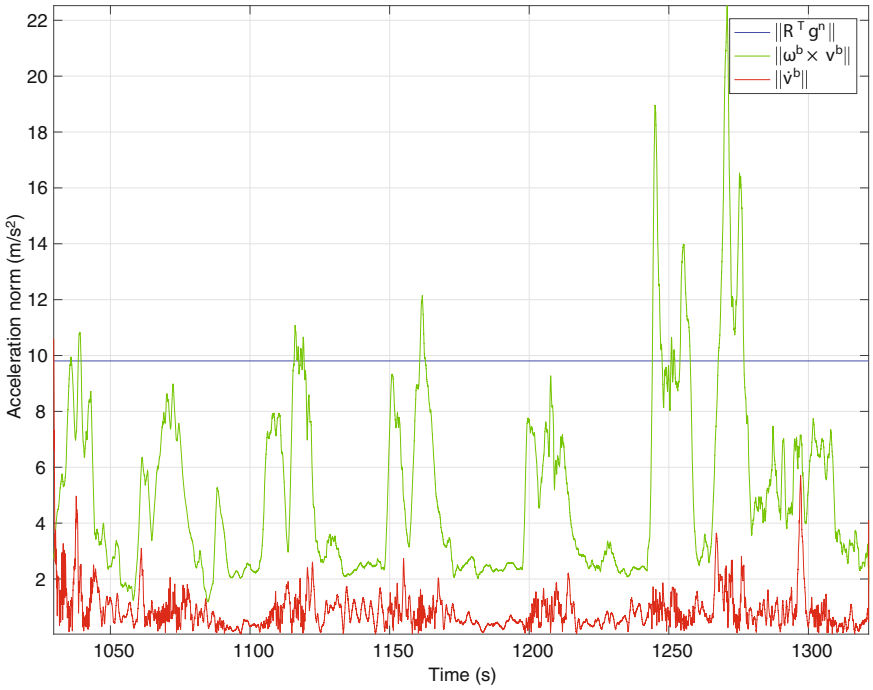

Fig. 5 Comparison of the norms of the different acceleration components

of the UAV: toward the end there are higher peaks because the UAV was preparing for landing and needed to perform some particularly sharp turns.

A more compact form for (14)–(15) is

$$\dot{x}(t) = f(x(t), t) + G(t)\, n_x(t) \tag{17a}$$
$$y(t) = h(x(t), t) + E(t)\, n_y(t) \tag{17b}$$

where f, G, and E are smooth vector- and matrix-valued functions, x represents the state vector, y the output, t the time, and n_x and n_y are vectors of process and measurement noise, respectively. Let $\bar{x}$ be an estimate for x, and assume it is bounded as given by a global NLO, with bounded error $\breve{x} = x - \bar{x}$. A first-order Taylor series expansion of (17) about $\bar{x}(t)$ gives

$$\dot{x}(t) = f(\bar{x}(t), t) + F(\bar{x}(t), t)\, \breve{x}(t) + G(t)\, n_x(t) + q_1(x(t), \bar{x}(t), t) \tag{18a}$$
$$y(t) = h(\bar{x}(t), t) + H(\bar{x}(t), t)\, \breve{x}(t) + E(t)\, n_y(t) + q_2(x(t), \bar{x}(t), t) \tag{18b}$$

where $q_1(x(t), \bar{x}(t), t)$ and $q_2(x(t), \bar{x}(t), t)$ are higher order terms and

$$F(\bar{x}(t), t) = \frac{\partial f}{\partial x}(\bar{x}(t), t) \tag{19}$$

$$H(\bar{x}(t), t) = \frac{\partial h}{\partial x}(\bar{x}(t), t). \tag{20}$$

Building up from the theory in [19], an estimator $\hat{x}$ for x is then

$$\dot{\hat{x}}(t) = f(\bar{x}(t), t) + F(\bar{x}(t), t)\, x_d(t) + K(t)(y(t) - h(\bar{x}(t), t) - H(\bar{x}(t), t)\, x_d(t)), \tag{21}$$

where $x_d(t) = \hat{x}(t) - \bar{x}(t)$. Recall that the Kalman filter is optimal if n_x is Gaussian white noise with covariance matrix Q, n_y is Gaussian white noise with covariance matrix U, and n_x and n_y are uncorrelated. The gain matrix K can then be calculated as $K(t) = P(t)H(\bar{x}(t), t)^T U^{-1}$, with P the time-varying solution of the Riccati equation

$$\dot{P}(t) = F(\bar{x}(t), t)P(t) + P(t)F^T(\bar{x}(t), t) + G(t)QG^T(t) - K(t)UK^T(t) \tag{22}$$

The state estimation error is $\tilde{x} := x - \hat{x} = \breve{x} - \hat{x} - \bar{x}$. Combining (18) and (21) yields a linear time-varying system with a perturbation:

$$\dot{\tilde{x}}(t) = A(\bar{x}(t), t)\tilde{x}(t) + d(t), \tag{23}$$

where

$$A(\bar{x}(t), t) = F(\bar{x}(t), t) - K(t)H(\bar{x}(t), t) \tag{24}$$

$$d(t) = G(t)n_x + q_1(x(t), \bar{x}(t), t) + K(t)q_2(x(t), \bar{x}(t), t) + K(t)E(t)n_y. \tag{25}$$

The following assumptions are standard conditions that ensure boundedness and positive definiteness of the solution of the Riccati equation, and lead to nominal global convergence of the Kalman filter [1, 22].

Assumption 4 The LKF tunable parameters $P(0)$, Q, and U are positive definite and symmetric.

Assumption 5 The system $(F(\bar{x}(t), t), G(t), H(\bar{x}(t), t))$ is uniformly completely observable and controllable.

Stability of the XKF

The next theorem gives condition that ensure stability of the XKF.

Theorem 2 *Suppose Assumptions 1–5 hold. The origin $\breve{x} = \tilde{x} = 0$ of the unforced error dynamics of the cascade (8)–(9) and (17), i.e., of the XKF (with $n_x = 0$ and $n_y = 0$), inherits the stability properties of the NLO.*

Proof By joining Assumptions 4 and 5 with the global exponential stability of the NLO, the conclusions of the theorem follow from Theorem 2.1 in [19]. □

Assumptions 1–3 are necessary for global exponential stability of the NLO. Assumption 4 can be satisfied by design. The requirements of Assumption 5 are hard to verify analytically a-priori. However, it is possible to calculate the observability and controllability Gramians recursively at runtime, and since they always result full rank, it can be inferred that Assumption 5 is satisfied.

If n_x and n_y are bounded inputs instead of zero, having a GES NLO allows to invoke Lemma 4.6 in [23], which implies that the origin of the error dynamics of the XKF is input-to-state stable with n_x and n_y as inputs, and that the solutions are uniformly ultimately bounded.

The stability properties of the XKF are inherited from the NLO, while the advantage over the NLO is the use of minimum-variance objectives in the design of the estimator. The linearization introduced with the LKF, however, creates an inevitable, possibly biased, random error that might lead to suboptimality and is hard to analyze in an experimental scenario. The best option in such cases is to resort to simulations to investigate the structure of the error.

5 Results

The XKF is here tested on both experimental and simulated data. Root mean square (RMS) errors are presented for both cases. In addition, a case study is presented to test the viability of the NLO with different reference vectors, should the camera system fail to provide useful OF estimates.

Fig. 6 The UAV Factory Penguin-B on the runway with the pilot, just before the experiment

5.1 Experimental Setup and Results

The UAV employed is a UAV Factory Penguin-B (Fig. 6), equipped with a custom payload that includes all the necessary sensors. The IMU is a Sensonor STIM300, a low-weight, tactical grade, high-performance sensor that includes gyroscopes, accelerometers, and inclinometers, all recorded at a frequency of 300 Hz. The chosen GPS receiver is a uBlox LEA-6T, which gives measurements at 5 Hz. The video camera is an IDS GigE uEye 5250CP provided with an 8 mm lens. The camera is configured for a hardware-triggered capture at 10 Hz: the uBlox sends a digital pulse-per-second signal whose rising edge is accurately synchronized with the time of validity of the recorded GPS position, which guarantees that the image capture is synchronized with the position measurements. The experiment has been carried out on February 6, 2015 at the Eggemoen Aviation and Technology Park, Norway, in a sunny day with good visibility, very little wind, an air temperature of about -8°C. The terrain is covered with snow and flat enough to let all features be considered as lying at zero altitude relative to altitude measurements.

In order to produce OF vectors, all the camera images are processed with a resolution of 1600 × 1200 (width × height) pixels and in their original state, without any filtering. The lens distortion of the camera is not accounted for, and no correction is applied to the images. SIFT is implemented with the open source computer vision library (OpenCV) [5] with default settings. Each match is tagged with a value indicating the accuracy of the match, and the smallest of these values is considered to be the best match. To increase the reliability of the OF vectors, each match is compared to the best one. Every match with an uncertainty more than double the uncertainty of the best match is not used. Also the template matching algorithm is implemented with OpenCV. The size of the templates is chosen to be 120 × 90 pixels and a correlation of 99% is required in order for a template match to be considered reliable and used.

The NLO is implemented using forward Euler discretization with a time-varying step depending on the interval of data acquisition of the fastest sensor, namely the STIM300, and it is typically around 0.003 seconds. The various parameters and gains are chosen as $L_{b^b} = 2°/\text{s}$, $L_{\hat{b}^b} = 2.1°/\text{s}$, $\sigma = 1$, $K_P = \text{diag}[0.08, 0.04, 0.06]$, $k_I = 0.02$, $K_{pp} = 30I_3$, $K_{pv} = 2I_3$, $K_{vp} = 0.01I_3$, $K_{vv} = 20I_3$, $K_{\xi p} = I_3$, and $K_{\xi v} = 50I_3$. All the gains are obtained by running the NLO several times and correcting the gains until a satisfactory performance was achieved. The gyro bias estimates are initialized with the standstill values, the other states with zero.

The covariance matrices Q and U are first tuned based on previous experience with the same sensors and system model, and then more finely tuned with trial and error. In both XKF and EKF, all estimates have zero initial value.

The reference provided for the position, velocity, and attitude is the output of the EKF of the autopilot mounted on the Penguin-B; the autopilot uses a different set of sensors than the one presented here. The path flown by the UAV and its NED velocity are in Figs. 7 and 8. An exact reference for the gyro bias is not available, but an approximation of the real value is calculated by averaging the gyro measurements

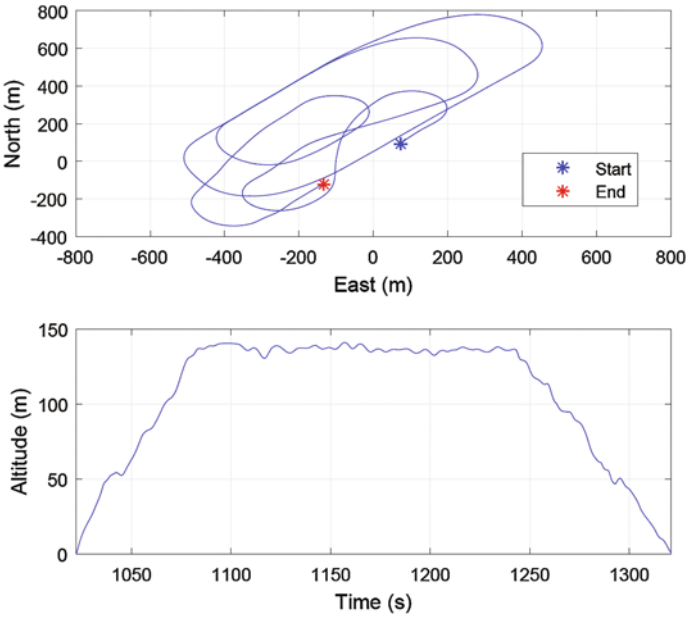

Fig. 7 Path of the UAV during the experiment. The zero is the base station from where the UAV was controlled

at standstill before and after the flight. The accelerometer bias is not estimated, but it is computed the same way as the gyro bias and subtracted from the accelerometers measurements before being used in the XKF (Figs. 7 and 8).

Ignoring for the sake of readability the time parameters, the equations implemented to run the discrete LKF in the XKF are

$$
\begin{aligned}
K &= \bar{P}H(\bar{x})[H(\bar{x})\bar{P}H^T(\bar{x})]^{-1} \\
\hat{x} &= x_t + K[y - \bar{y} - H(\bar{x})(\hat{x} - \bar{x})] \\
\hat{P} &= [I - KH(\bar{x})]\bar{P}[I - KH(\bar{x})]^T + KUK^T \\
x_t &= \hat{x} + h[f(\bar{x}) + F(\bar{x})(\hat{x} - \bar{x})] \\
\Phi &= I + hF(\bar{x}) \\
\Gamma &= hE \\
\bar{P} &= \Phi\hat{P}\Phi^T + \Gamma Q\Gamma^T
\end{aligned}
$$

Figures 9, 10, 11 and 12 display the estimation errors of the NLO alone, of the entire XKF, and of an EKF with the same tuning parameters and initialization as the XKF. The time on the x-axes is the time elapsed since starting up the UAV; the dataset represented corresponds to the entire flight of the UAV. The RMS errors are reported in Table 1. All estimators converge, as expected, and the XKF and EKF perform better than the NLO.

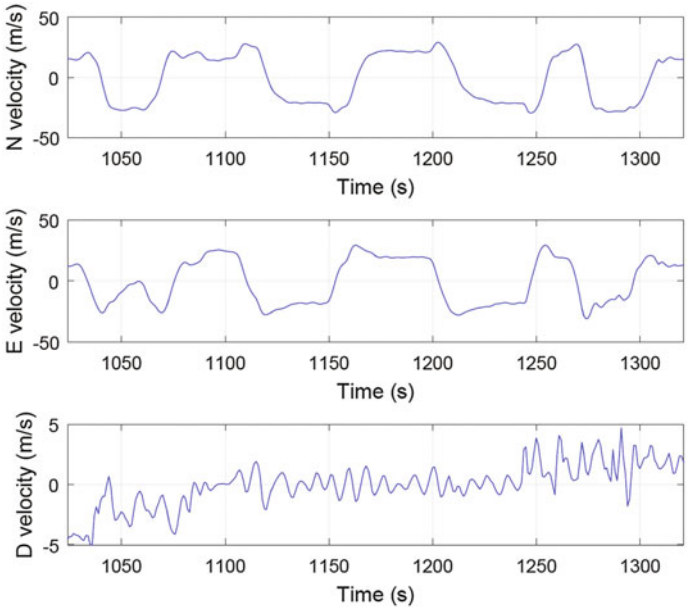

Fig. 8 NED velocity of the UAV during the experiment

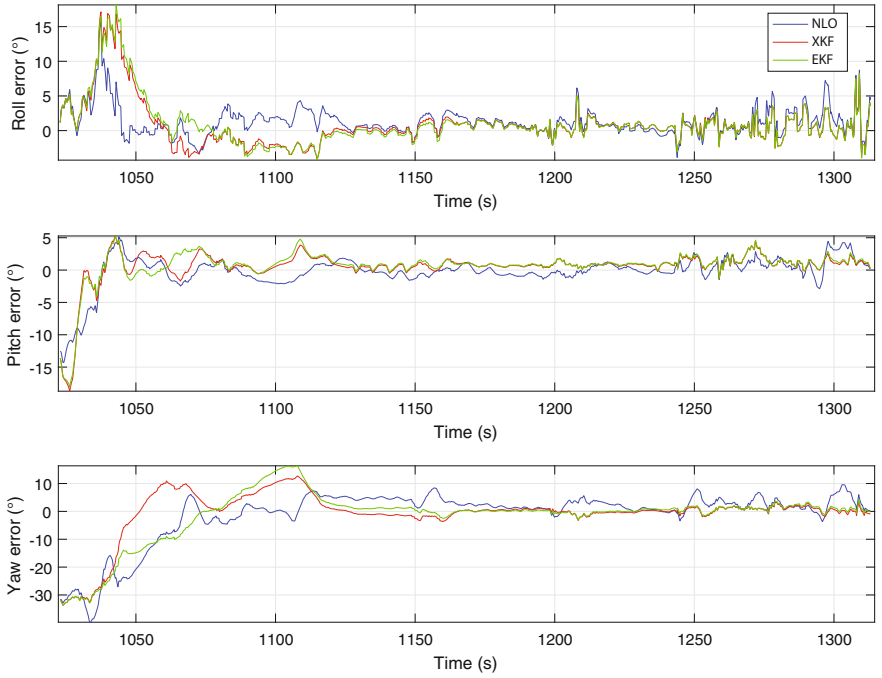

Fig. 9 Euler angles estimation error of the three methods with respect to the autopilot EKF

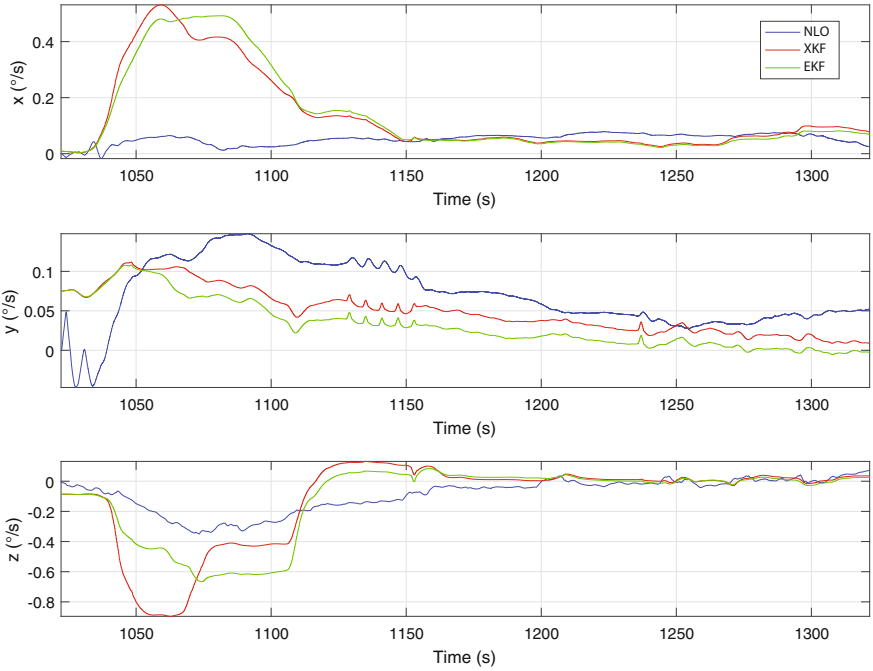

Fig. 10 Gyro bias estimation error of the three methods with respect to the autopilot EKF

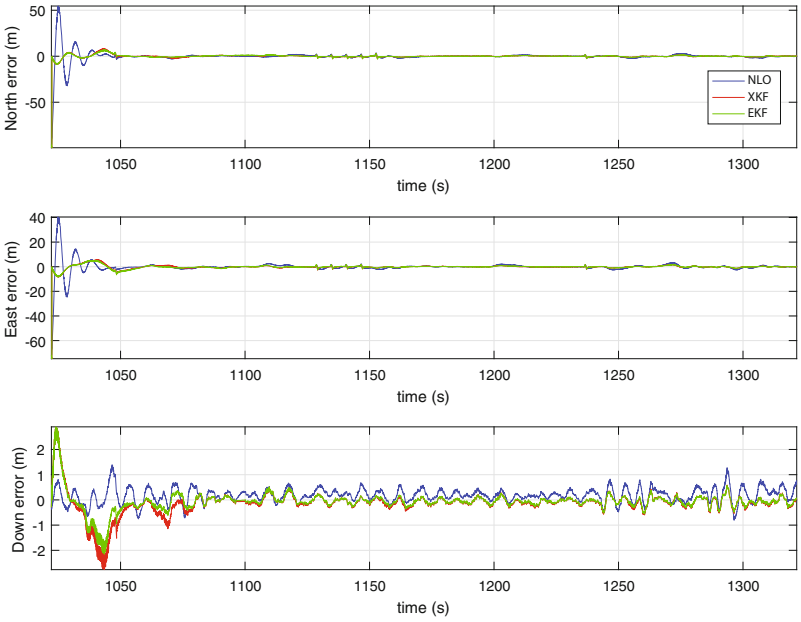

Fig. 11 NED position estimation error of the three methods with respect to the autopilot EKF

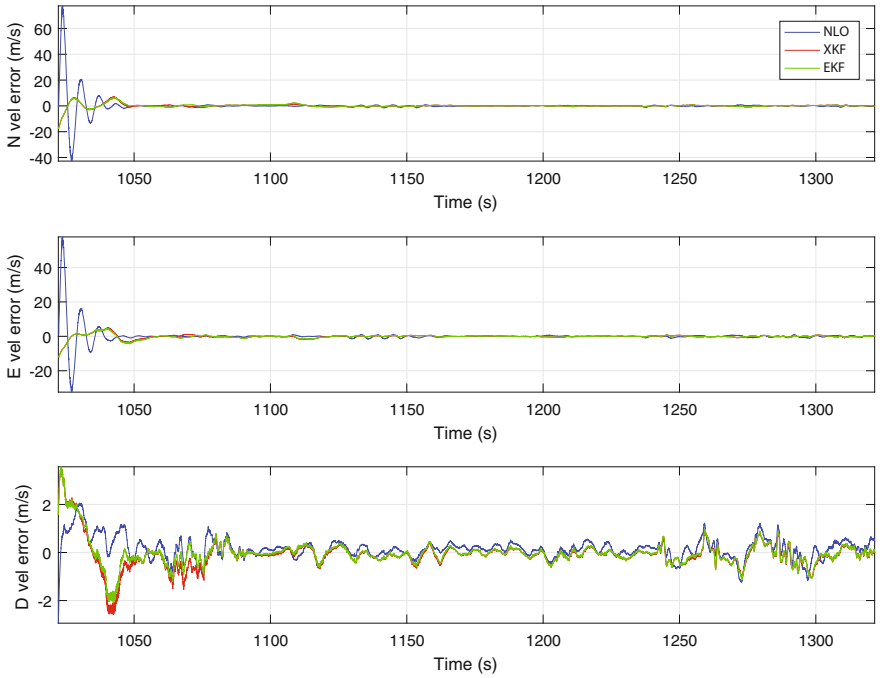

Fig. 12 NED velocity estimation error of the three methods with respect to the autopilot EKF

Table 1 RMS errors for the experimental data

State	NLO	XKF	EKF
Roll ϕ (°)	1.887	1.363	1.355
Pitch θ (°)	1.319	1.265	1.336
Yaw ψ (°)	0.055	0.018	0.021
Gyro bias x (°/s)	0.065	0.059	0.051
Gyro bias y (°/s)	0.049	0.030	0.012
Gyro bias z (°/s)	0.028	0.019	0.019
North position (m)	0.876	0.417	0.419
East position (m)	0.944	0.449	0.440
Down position (m)	0.330	0.176	0.156
North velocity (m/s)	0.291	0.286	0.257
East velocity (m/s)	0.352	0.285	0.251
Down velocity (m/s)	0.374	0.313	0.314

Another term of comparison for the estimators is their behavior with large initialization errors. If, for example, the estimators are initialized with large attitude estimation errors, the EKF yaw estimation error does not converge to zero, whereas NLO and XKF converge due to their GES property.

There is no guarantee that the EKF onboard the autopilot is the device that gives the best estimates with respect to the real, unknown values. For this reason, a simulation is run in order to have access to perfect measurements of the states.

5.2 *Simulation Setup and Results*

The simulated flight has several changes of direction and slight changes in altitude. Instead of simulating the entire machine vision system, a body velocity sensor is simulated by adding Gaussian white noise to the known, exact value. The GPS-measured position and velocity are modeled as Gauss–Markov processes with added Gaussian white noise, according to the specifications in [4]. Gaussian white noise is added to all the other sensors too, with standard deviations 0.135 deg/s for the rate gyros, 0.02 m/s^2 for the accelerometers, and 0.3 m/s for the body-fixed velocity. A constant bias is added to the gyro measurements.

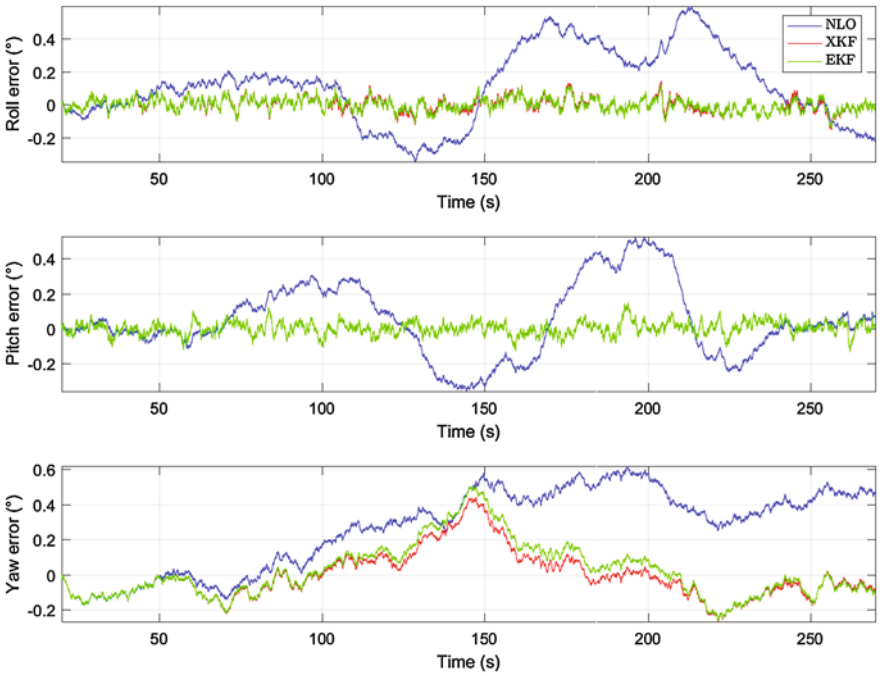

Fig. 13 Euler angles estimation error of the three methods with simulated data

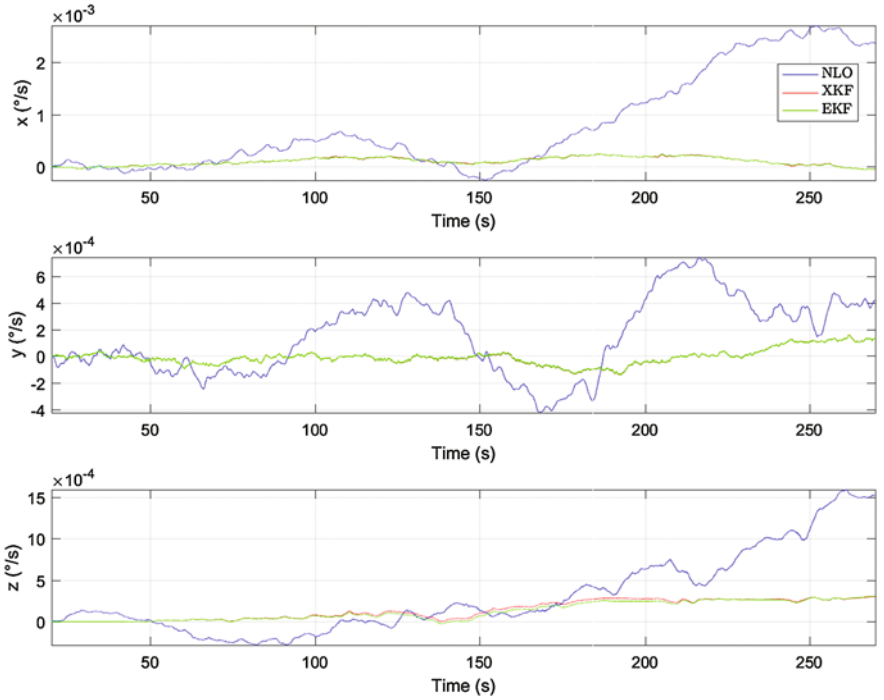

Fig. 14 Gyro bias estimation error of the three methods with simulated data

Table 2 RMS errors for the simulation

State	NLO	XKF	EKF
Roll ϕ (°)	0.288	0.044	0.040
Pitch θ (°)	0.127	0.039	0.039
Yaw ψ (°)	0.397	0.126	0.121
Gyro bias x (°/s)	0.002	1.24e–04	1.23e–03
Gyro bias y (°/s)	4.69e–04	8.22e–05	8.15e–05
Gyro bias z (°/s)	0.001	2.69e–04	2.66e–04
North position (m)	0.189	0.153	0.153
East position (m)	0.179	0.146	0.141
Down position (m)	0.310	0.274	0.276
North velocity (m/s)	0.219	0.047	0.044
East velocity (m/s)	0.226	0.051	0.053
Down velocity (m/s)	0.359	0.047	0.047

The results are in Fig. 13, 14, 15 and 16 and the RMS errors in Table 2. It is clear that the NLO performs worse than the XKF and EKF, and it is particularly evident in the position and velocity estimates that the NLO estimates have more noise.

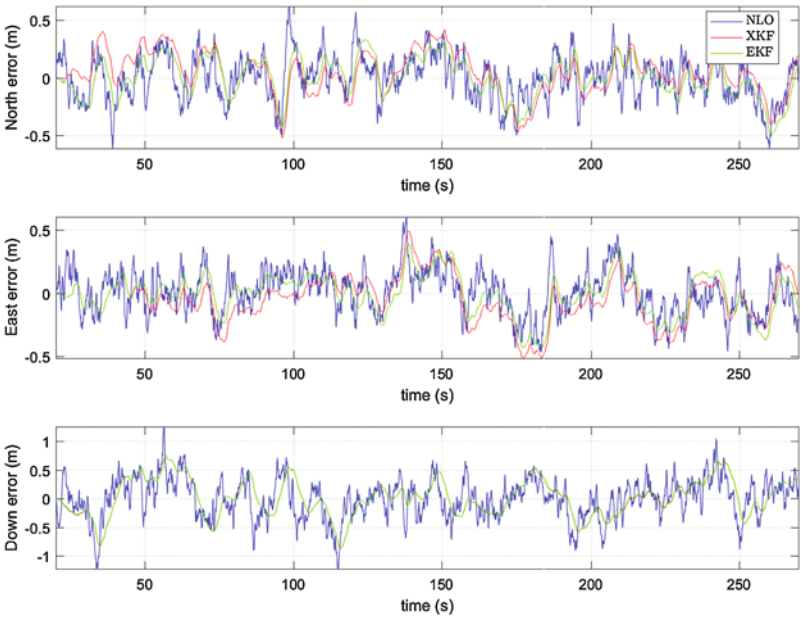

Fig. 15 NED position estimation error of the three methods with simulated data

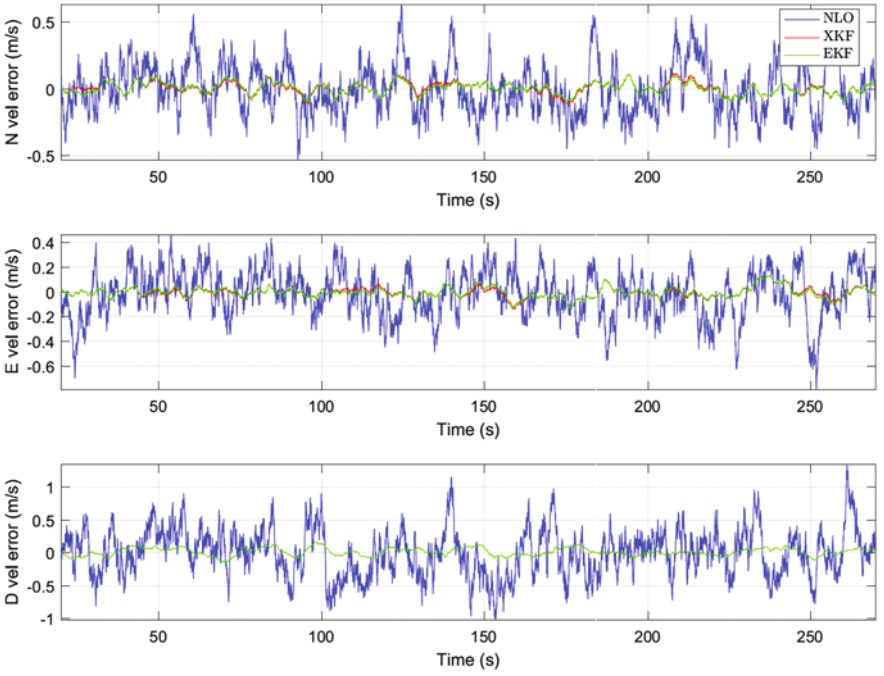

Fig. 16 NED velocity estimation error of the three methods with simulated data

Table 3 RMS errors for the NLO using acceleration and heading from GPS

State	NLO
Roll ϕ (°)	2.681
Pitch θ (°)	1.965
Yaw ψ (°)	0.391
Gyro bias x (°/s)	0.053
Gyro bias y (°/s)	0.124
Gyro bias z (°/s)	0.275
North position (m)	0.883
East position (m)	0.915
Down position (m)	0.306
North velocity (m/s)	0.852
East velocity (m/s)	0.687
Down velocity (m/s)	0.365

5.3 Case Study: Camera or OF Failure

A fundamental component of the NLO is the body-referenced velocity obtained via machine vision. If the camera optical flow algorithm fails to function, the velocity becomes unreliable and a new solution is necessary. The acceleration vectors alone can help estimate the roll and pitch angles, whereas the yaw requires an additional pair of vectors. Assuming that the course and heading of the UAV coincide, the v^b and v^n vectors in the injection term can be replaced by

$$m^n = \begin{bmatrix} 1 \\ 0 \\ 0 \end{bmatrix}, \qquad m^b = \begin{bmatrix} \cos(\psi) \\ -\sin(\psi) \\ 0 \end{bmatrix} \approx \frac{1}{\|v^n\|} \begin{bmatrix} v_N^n \\ -v_E^n \\ 0 \end{bmatrix} \tag{26}$$

The vector m^b is then calculated based on the GPS velocity readings. This solution is clearly not ideal, for it would yield inaccurate results in the presence of strong crosswinds leading to a crab angle, but it would work as a degraded accuracy mode.

The method is tested on the same experimental data used in Sect. 5.1. The RMS error is in Table 3. Plots are not presented due to lack of space. The results are in general worse than those obtained using the camera, as expected, but would still be a viable solution.

6 Conclusions

This chapter presented the results and experimental verification of the exogenous Kalman filter for the estimation of a fixed-wing UAV navigation states. The theory

behind the filter was presented, with theorems proving the global exponential stability properties of the method, followed by the experimental results, where the estimates from the nonlinear observer, exogenous Kalman filter, and extended Kalman filter were compared with the output (an extended Kalman filter itself) of the autopilot onboard the UAV. The two Kalman filter solutions have better noise rejection, and they were also tested on simulated data in order to be able to compare the estimates with perfect reference values. Moreover, unlike the EKF, the XKF has proven GES properties. An additional case study was presented to provide a degraded accuracy solution in case of a camera failure, and allow the UAV to land safely.

Acknowledgements This work was partly supported by the Norwegian Research Council (grant numbers 225259 and 223254) through the Center of Autonomous Marine Operations and Systems at the Norwegian University of Science and Technology.
The authors are grateful for the assistance provided by the UAV engineers at NTNU and Maritime Robotics AS, in particular Lars Semb and Carl Erik Stephansen. Significant contributions were made to the construction of the UAV payload by the rest of the navigation team at NTNU, in particular Sigurd M. Albrektsen, Jakob M. Hansen and Kasper T. Borup, and to the development of machine vision by Jesper Hosen and Håkon H. Helgesen.

Appendix

The parameter projection $\text{Proj}(\cdot, \cdot)$ is defined as

$$\text{Proj}(\hat{b}^b, \tau) = \begin{cases} \left(I - \frac{c(\hat{b}^b)}{\|\hat{b}^b\|^2} \hat{b}^b \hat{b}^{bT}\right) \tau, & \|\hat{b}^b\| \geq L_b, \ \hat{b}^{bT} \tau > 0 \\ \tau, & \text{otherwise} \end{cases}$$

where $c(\hat{b}^b) = \min\{1, (\|\hat{b}^b\|^2 - L_b^2)/(L_{\hat{b}}^2 - L_b^2)\}$. This operator is a special case of that from Appendix E of [24]. Some of its properties are reported here: (i) $\text{Proj}(\cdot, \cdot)$ is locally Lipschitz continuous, (ii) $\|\hat{b}^b\| \geq L_{\hat{b}} \Rightarrow \hat{b}^{bT} \text{Proj}(\hat{b}^b, \tau) \leq 0$, (iii) $\|\text{Proj}(\hat{b}^b, \tau)\| \leq \|\tau\|$, and (iv) $-\tilde{b}^{bT} \text{Proj}(\hat{b}^b, \tau) \leq -\tilde{b}^{bT} \tau$.

References

1. Anderson, B.D.O.: Stability properties of Kalman-Bucy filters. J. Frankl. Inst. **291**, 137–144 (1971)
2. Batista, P., Silvestre, C., Oliveira, P.: A GES attitude observer with single vector observations. Automatica **48**(2), 388–395 (2012)
3. Batista, P., Silvestre, C., Oliveira, P.: Globally exponentially stable cascade observers for attitude estimation. Control Eng. Pract. **20**, 148–155 (2012)
4. Beard, R.W., McLain, T.W.: Small Unmanned Aircraft: Theory and Practice. Princeton University Press, Princeton (2012)
5. Bradski, G.: The OpenCV library. Dr. Dobbs J. **25**(11), 120–126 (2000)

6. Brown, R.G., Hwang, P.Y.C.: Introduction to Random Signals and Applied Kalman Filtering, 3rd edn. Wiley, London (2012)
7. Fossen, T.I.: Handbook of Marine Craft Hydrodynamics and Motion Control. Wiley, London (2011)
8. Fuh, C.S., Maragos, P.: Region-based optical flow estimation. IEEE Comput. Soc. Conf. Comput. Vis. Pattern Recognit. 130–135 (1989)
9. Fusini, L., Johansen, T.A., Fossen, T.I.: Experimental validation of a uniformly semi-globally exponentially stable non-linear observer for GNSS- and camera-aided inertial navigation for fixed-wing UAVs. In: Proceedings of the International Conference on Unmanned Aircraft Systems (2015). doi:10.1109/ICUAS.2015.7152371
10. Gelb, A.: Applied Optimal Estimation. MIT Press, Cambridge (1974)
11. Grip, H.F., Fossen, T.I., Johansen, T.A., Saberi, A.: Attitude estimation using biased Gyro and vector measurements with time-varying reference vectors. IEEE Trans. Autom. Control **57**(5), 1332–1338 (2012)
12. Grip, H.F., Fossen, T.I., Johansen, T.A., Saberi, A.: Globally exponentially stable attitude and gyro bias estimation with application to GNSS/INS integration. Automatica **51**, 158–166 (2015)
13. Gustafsson, F.: Statistical Sensor Fusion, Studentliteratur AB, Lund, Sweden (2012)
14. Hosen, J., Helgesen, H.H., Fusini, L., Fossen, T.I., Johansen, T.A.: Vision-aided nonlinear observer for fixed-wing unmanned aerial vehicle navigation. J. Guidance Control Dyn. **39**(8), 1777–1789 (2016)
15. Hua, M.D., Martin, P., Hamel, T.: Stability analysis of velocity-aided attitude observers for accelerated vehicles. Automatica **63**, 11–15 (2016)
16. Hutchinson, S., Hager, G.D., Corke, P.I.: A tutorial on visual servo control. IEEE Trans. Robot. Autom. **12**(5), 651–670 (1996)
17. Johansen, T.A., Fossen, T.I.: Nonlinear observer for tightly coupled integration of pseudo-range and inertial measurements. IEEE Trans. Control Syst. Technol. **24**, 2199–2206 (2016). doi:10.1109/TCST.2016.2524564
18. Johansen, T.A., Fossen, T.I.: Nonlinear filtering with eXogenous Kalman filter and double Kalman Filter. In: European Control Conference, Aalborg (2016)
19. Johansen, T.A., Fossen, T.I.: The eXogenous Kalman Filter (XKF). Int. J. Control (2016). doi:10.1080/00207179.2016.1172390
20. Johansen, T.A., Fossen, T.I., Goodwin, G.C.: Three-stage filter for position estimation using pseudo-range measurements. IEEE Trans. Aerosp. Electron. Syst. **52**, 1631–1643 (2016)
21. Julier, S.J., Uhlmann, J.K.: Unscented filtering and nonlinear estimation. Proc. IEEE **92**(3), 401–422 (2004)
22. Kalman, R.E., Bucy, R.S.: New results in linear filtering and prediction theory. Trans. ASME Ser. D J. Basic Eng. **83**, 95–109 (1961)
23. Khalil, H.K.: Nonlinear Systems. Prentice-Hall, Englewood Cliffs (2002)
24. Krstic, M., Kanellakopoulos, I., Kokotovic, P.V.: Nonlinear and Adaptive Control Design. Wiley, New York (1995)
25. Loria, A., Panteley, E.: Cascaded nonlinear time-varying systems: analysis and design. In: Lamnabhi-Lagarrigue, F., Loria, A., Panteley, E. (eds.) Advanced Topics in Control Systems Theory, pp. 23–64. Springer, London (2004)
26. Lowe, D.G.: Object recognition from local scale-invariant features. In: Proceedings of the International Conference on Computer Vision, pp. 1150–1157 (1999)
27. Luenberger, D.G.: Observing a state of a linear system. IEEE Trans. Mil. Electron. **8**, 74–80 (1964)
28. Mahony, R., Hamel, T., Pflimlin, J.M.: Nonlinear complementary filters on the special orthogonal group. IEEE Trans. Autom. Control **53**(5), 1203–1218 (2008)
29. Mammarella, M., Campa, G., Fravolini, M.L., Napolitano, M.R.: Comparing optical flow algorithms using 6-DOF motion of Real-World rigid objects. IEEE Trans. Syst. Man Cybern. Part C: Appl. Rev. **42**(6), 1752–1762 (2012)

30. Martin, P., Salaun, E.: Design and implementation of a low-cost observer-based attitude and heading reference system. Control Eng. Pract. **18**(7), 712–722 (2010)
31. Panteley, E., Loria, A.: On global uniform asymptotic stability of nonlinear time-varying systems in cascade. Sys. Control Lett. **33**, 131–138 (1998)
32. Reif, K., Sonnemann, F., Unbehauen, R.: An EKF-based nonlinear observer with a prescribed degree of stability. Automatica **34**, 1119–1123 (1998)
33. Salcudean, S.: A globally convergent angular velocity observer for rigid body motion. IEEE Trans. Autom. Control **36**(12), 1493–1497 (1991)
34. Sarvaiya, J.N., Patnaik, S., Bombaywala, S.: Image registration by template matching using normalized cross-correlation. In: International Conference Advances in Computing, Control, and Telecommunication Technologies (2009). doi:10.1109/ACT.2009.207
35. Shuster, M.D., Oh, S.D.: Three-axis attitude determination from vector observations. J. Guid. Control Dyn. **4**(1), 70–77 (1981)
36. Simon, D.: Optimal State Estimation: Kalman, H Infinity, and Nonlinear Approaches. Wiley, London (2006)
37. Song, Y., Grizzle, J.W.: The extended Kalman filter as a local asymptotic observer for discrete-time nonlinear systems. J. Math. Syst. Estim. Control **5**, 59–78 (1995)
38. Sonka, M., Hlavac, V., Boyle, R.: Image Processing, Analysis, and Machine Vision. Cengage Learning, Stamford (2008)
39. Stovner, B., Johansen, T.A., Fossen, T.I., Schjølberg, I.: Three-stage filter for position and velocity estimation from long baseline measurements with unknown wave speed. In: American Control Conference, Boston (2016)

http://www.springer.com/978-3-319-55371-9

Sensing and Control for Autonomous Vehicles
Applications to Land, Water and Air Vehicles
Fossen, T.I.; Pettersen, K.Y.; Nijmeijer, H. (Eds.)
2017, IX, 518 p. 212 illus., 170 illus. in color., Hardcover
ISBN: 978-3-319-55371-9